Astronomy & Astrophysics

XMM-Newton long-look observation of the narrow line Seyfert 1 galaxy PKS 0558−504

I. Spectral analysis

I. E. Papadakis[1,2], W. Brinkmann[3], M. Gliozzi[4], C. Raeth[3], F. Nicastro[2,5,6], and M. L. Conciatore[6]

[1] Physics Department, University of Crete, PO Box 2208, 710 03 Heraklion, Crete, Greece
    e-mail: jhep@physics.uoc.gr
[2] IESL, Foundation for Research and Technology, 711 10, Heraklion, Crete, Greece
[3] Max-Planck-Institut für extraterrestrische Physik, Giessenbachstrasse, 85740 Garching, Germany
[4] George Mason University, Department of Physics and Astronomy, MS 3F3, 4400 University Dr., Fairfax, VA 22030, USA
[5] Osservatorio Astronomico di Roma, INAF, Italy
[6] Harvard-Smithsonian Center for Astrophysics, 60 Garden Street, Cambridge, MA 02138, USA

ABSTRACT

Context. PKS 0558-504 has been observed repeatedly by *XMM-Newton* as a calibration and performance verification (PV) target. In this work, we present results from the spectral analysis of a long XMM-Newton observation of the radio loud Narrow Line Seyfert 1 galaxy PKS 0558-504.
Aims. To study the soft excess component in this object, the spectral variations it exhibits in both the hard and soft X-ray bands, and their correlation.
Methods. We used mainly the PN data, and we fitted various spectral models to the time average spectra of the individual orbits as well as the spectra from data segments of shorter duration. We also used the RGS data to search for signs of a warm absorber in the source.
Results. The source is highly variable, on all sampled time scales. We did not observe any absorption features in either the soft or hard band. We found weak evidence for the presence of an iron line at ∼6.8 keV, which is indicative of emission from highly ionized iron. The 2–10 keV band spectrum of the source is well fitted by a simple power law model, whose slope steepens with increasing flux, similar to what is observed in other Seyferts as well. The soft excess is variable both in flux and shape, and it can be well described by a low-temperature Comptonisation model, whose slope flattens with increasing flux. Finally, the soft excess flux variations are moderately correlated with the hard band variations, and we found weak evidence that they are leading them by ∼20 ks.
Conclusions. Our results rule out a jet origin for the bulk of the X-ray emission in this object. We found no signals of a warm absorber. The observed hard band spectral variations suggest intrinsic continuum slope variations, caused by changes in the "heating/cooling" ratio of the hot corona. The low-temperature Comptonising medium, responsible for the soft excess emission, could be a hot layer in the inner disc of the source, which appears due to the fact that the source is accreting at a super-Eddington rate. The soft excess flux and spectral variations could be caused by random variations of the accretion rate.

Key words. galaxies: active – galaxies: Seyfert – X-rays: galaxies

1. Introduction

Narrow Line Seyfert 1 galaxies (NLS1) are optically identified by their emission line properties: the ratio of [O III]/Hβ is less than 3 and the FWHM Hβ less than 2000 km s^{-1} (Osterbrock & Pogge 1985; Goodrich 1989). Their optical spectra are further characterised by the presence of strong permitted Fe II, Ca II, and O I λ 8446 ionisation lines (Persson 1988). NLS1 have been rarely found to be radio-loud (Ulvestad et al. 1995; Siebert et al. 1999; Grupe et al. 1999). Recent dedicated studies, in particular using the Sloan digital sky survey, demonstrated that this is a consequence of the low radio-loud fraction of the NLS1 population (∼7%, Komossa et al. 2006). The same authors found that radio-loud NLS1 galaxies resemble GHz-peaked/compact steep spectrum sources, and Yuan et al. (2008) suggested similarities with high-energy peaked BL Lac Objects.

PKS 0558-504 ($z = 0.1372, m_B = 14.97$) is one of the best studied radio loud NLS1 galaxies ($R_L = f_{5\,\mathrm{GHz}}/f_B \simeq 27$;

Siebert et al. 1999). A peculiar property displayed by the source is its unusually high X-ray to radio luminosity ratio (Brinkmann et al. 1997). It was optically identified on the basis of its X-ray position from HEAO-1 (Remillard et al. 1986). It is an X-ray bright source, with a flux of ∼1.5−2 × 10^{-11} erg cm^{-2} s^{-1} in the 2–10 keV band. Its 2–10 keV spectrum is rather steep ($\Gamma \sim 2.2$; Gliozzi et al. 2007). Its spectral slope remains roughly constant on long time scales, despite the large amplitude flux variations that the source exhibits (Gliozzi et al. 2007). PKS 0558-504 also exhibits strong flux variations on short time scales (Remillard et al. 1991; Gliozzi et al. 2000, 2001; Wang et al. 2001; Brinkmann et al. 2004).

PKS 0558-504 has been observed repeatedly by *XMM-Newton* as a calibration and performance verification (PV) target. O'Brien et al. (2001) published the spectral analysis of some preliminary data of the commissioning/CalPV phase. The 0.2−2 keV spectrum was dominated by a large soft X-ray excess, which showed no evidence for absorption

or emission line features and was fitted by a model consisting of three black body components. An analysis of all PV phase and calibration observations performed by *XMM-Newton* up to orbit 341, with various instrumental settings, was presented by Brinkmann et al. (2004). They found that all spectra could be well fitted by two Comptonisation components, one at moderate temperatures of $kT \sim 4.5$ keV and optical depths of $\tau \sim 2$, the other at high temperatures ($kT \gtrsim 50$ keV) and low optical depths ($\tau \lesssim 1.0$). The same *XMM-Newton* data were recently used by Haba et al. (2008). The spectra were fitted with a multicolour disc black body model (Mitsuda et al. 1984) plus a high energy power law. The results were interpreted in terms of a super-critical accretion flow with significant photon trapping in the inner regions of the accretion disc.

In September 2008, PKS 0558-504 was observed with *XMM-Newton* for five consecutive orbits. The main objective of this long observation was to study its X-ray flux variability and in particular to investigate whether it exhibits any quasi-periodic signals. The results from this study will be presented in a companion paper (Papadakis et al., in preparation). In this paper we present the results from the spectral analysis of the *XMM-Newton* data. We used mainly the PN data because of the higher sensitivity of the PN camera, although we sometimes resorted to the RGS and MOS data as well, mainly for clarification purposes. We start with the observational details in the next section. Section 3 deals with the spectral analysis of the PN data, first in the hard band and then for the total band. In the same section we also present the results from a preliminary analysis of the RGS data. Temporal spectral variations and a time resolved spectroscopic analysis are discussed in Sects. 4 and 5. We then present a more detailed analysis of the full band spectra in selected time intervals in Sect. 6. Finally, in Sect. 7 we summarise our results and we present a short discussion of their potential implications.

2. Observations and data analysis

PKS 0558-504 was observed with all instruments on board *XMM-Newton* for five consecutive orbits starting on 2008 September 9, 1:19 UT and ending on 2008 September 16, 12:02 UT. The observation identifiers range from 0555170201 (XMM revolution 1602) to 0555170601 (XMM revolution 1606). Below we will identify the individual observations by the last 3 digits (i.e. "obs-201", "obs-301", etc.). The PN was operated in Small Window mode (SW) with a thin filter, the MOS1 in Small Window mode with a thin filter, and the MOS2 in TIMING mode also thin filter. Both RGS were operated in spectroscopy mode.

For the following analysis we will rely mainly on data from the PN camera (Strüder et al. 2001) due to its superior statistical quality. The PN data have been processed using XMMSAS version 8.0. Source counts were accumulated from a rectangular box of 27×26 RAW pixels (1 RAW pixel $\sim 4.1''$) around the position of the source. Background data were extracted from a similar, source free region on the chip. We selected single and double events (PATTERN ≤ 4, FLAG = 0; for details of the instruments see Ehle et al. 2008). With an average count rate of about 10 cts s^{-1} photon pile-up is negligible for the PN detector, as verified using the XMMSAS task *epatplot*. The data were screened for high background in both the soft and hard bands. After rejection of time intervals affected by high background (usually at the end of the individual orbits) and flaring activity, the total useful observation time was 540 ks. For the spectral fits we employed for the PN the canned responses from the MPE database.

As for the RGS data, for each observation we used the tool *rgsproc* to extract calibrated first order spectra and responses for both RGS cameras. The RGS spectra are affected by numerous instrumental features due to hot pixels and/or bad columns in the read-out chips. To reduce the number of narrow spectral intervals blocked by such features, and their width, we modified the default *rgsproc* filtering parameters to exclude photons only from hot pixels and not from their neighbouring pixels. The RGS data can be affected by high particle background periods during parts of the *XMM-Newton* orbits, mostly caused by solar activity. The high energy band is the most affected by background flares, and high energy RGS photons are dispersed over the CCD-9 chip. We therefore extracted background light curves of the CCD-9 chip and selected as good-time-intervals of the processed observations only those during which the background count rate deviated by $\leq +2\sigma$ from the average background count rate of each observation. To improve and optimise the S/N of the RGS spectra, we then used the tool *rgscombine* to co-add the five RGS1 and RGS2 spectra. The final (after cleaning for high background time intervals) exposures of the RGS1 and RGS2 spectra are 480 ks and 466 ks, respectively.

The 0.4−10 keV PN light curve is shown in Fig. 1. The data, plotted in 100 s time bins, represent the actual count rate on the chip, i.e. they are not corrected for the live time of 0.71 of the SW mode. The source exhibits large amplitude flux variations on all sampled time scales. On long time scales, the source undergoes large intensity variations by a factor of ≤ 5 (from ~ 5 counts/s at the start of obs-201 to ~ 24 counts/s at the beginning of obs-601). On shorter time scales of the order of a few hours we still observe substantial and continuous variability with an amplitude of the order of ~ 2. A detailed analysis of the observed flux variations will be presented in a forthcoming paper.

3. Spectral analysis of the PN data

Previous studies of PKS 0558-504 have confirmed the presence of spectral components which are typical of the X-ray spectra of NLS1 galaxies: i) a strong soft excess below ~ 2 keV, which appears over the extrapolation of a higher energy power-law-like spectral component with a slope of $\sim 2-2.4$ (Gliozzi et al. 2000; O'Brien et al. 2001; Brinkmann et al. 2004), and ii) a smooth spectrum, with no obvious absorption and/or emission spectral features either at higher energies or in the soft band. Given the presence of the soft component, we first investigated the spectral shape of the source spectrum at energies above 2 keV. We then proceeded to study the full band energy spectrum.

For the spectral analysis, source counts were grouped with a minimum of 100 counts per energy bin. Spectral fits were performed with the XSPEC v.12.5.0 software package. The errors on the best-fitting model parameters represent the 90% confidence limits for one interesting parameter (unless otherwise stated). The energies of emission or absorption features are given in the rest frame of the source. We considered a model to provide an acceptable fit to the data if the quality of the fit is better than the 5% confidence level, and we accepted that the addition of a model component is significant if the quality of the fit is improved at more than the 95% confidence level. For the Galactic absorption we used the value of $N_H = 3.4 \times 10^{20}$ cm^{-2} (Kalberla et al. 2005).

3.1. High energy power law fits

We first considered the average spectrum from each individual *XMM-Newton* observation. A simple power law model (PL)
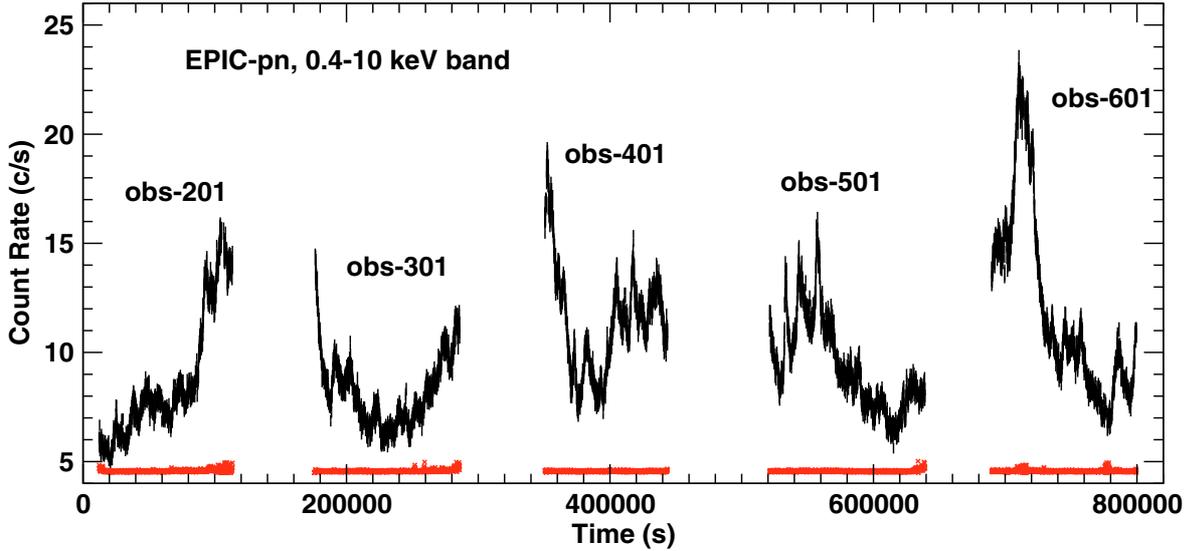
Fig. 1. The PN 0.4−10 keV light curve of PKS 0558-504 for all five observations with a binning of 100 s. The time counts from the beginning of the first observation. The points plotted with crosses at the bottom of the plot indicate the background count rate in the same energy range.
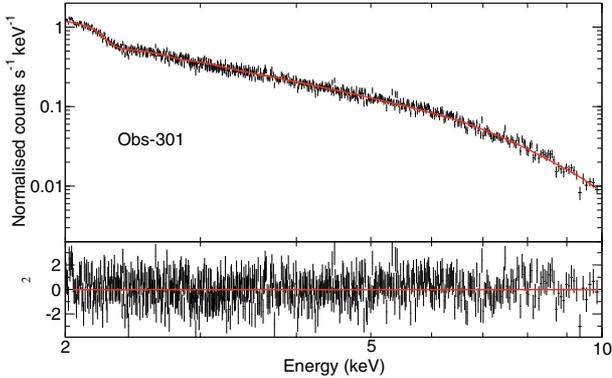

Fig. 2. *Top panel*: power law model fit to the total spectrum of obs-301 in the 2–10 keV band. *Lower panel*: the best-fit residuals plot (residuals are in terms of σ's with error bars of size one).

Table 1. Results from the PL model fits to the 2−10 keV average spectra of the 5 observations.

Obs.	Γ	2–10 keV Flux [†]	χ^2_{red}/d.o.f.
201	2.131 ± 0.015	9.53 ± 0.05	1.036/591
301	2.142 ± 0.014	9.07 ± 0.05	1.119/617
401	2.154 ± 0.011	13.0 ± 0.01	1.053/820
501	2.138 ± 0.012	11.2 ± 0.01	1.063/763
601	2.150 ± 0.011	13.9 ± 0.01	1.066/797

Notes. [†] In units of 10^{-12} erg cm^{-2} s^{-1}

fitted well the 2−10 keV spectrum of all observations, except for obs-301. That spectrum is rather noisy. Figure 2 shows the best power law model fit for this observation and the corresponding residuals. A broad, low-amplitude, line-like feature does appear close to ~6 keV (observers frame), but the addition of a Gaussian component did not improve the quality of the fit significantly (see the discussion in the next section). Possible absorption features also appear around ~7 keV. The addition of an EDGE component (in XSPEC terminology) to the model improved the fit (we got a reduction of $\Delta\chi^2$ of 24.8 for the addition of 2 degrees of freedom, d.o.f.), however, the best-fit edge energy turned out to be ~2.9 keV. It is difficult to spot this feature in Fig. 2, and we did not detect a similar feature in any of the average spectra of the other four observations. This fact casts doubt on the possibility that such an absorption edge is an intrinsic feature in the spectrum of the source.

The PL best-fit results are listed in Table 1. All spectra show a slope of $\Gamma \sim 2.13$−2.15. We did not observe significant indications of any absorption features in the high energy band spectra. We did not observe any spectral curvature in the hard energy band either. Nevertheless, a Comptonisation model (compTT in XSPEC, Titarchuk 1994) provided a nearly identical fit to the data. The main model parameters are the temperature, T_0, of the

soft photon input spectrum (which is assumed to be the Wien part of a black body), the electron plasma temperature, kT, and optical depth, τ. Their best fit values ($T_0 \sim 65$ eV, $kT \sim 50$ keV, and $\tau \sim 0.5$) are subject to large uncertainties due to their inherent degeneracy (in the absence of a the detection of the high energy cut-off) but, in any case, they are similar to those found for broad line Seyfert 1 galaxies (e.g. Petrucci et al. 2001).

The average 2−10 keV flux of the source during the *XMM-Newton* observations is $\sim 1.1 \times 10^{-11}$ erg cm^{-2} s^{-1}. This implies that PKS 0558-504 was at a rather low flux state, when compared to its average flux level of $\sim 1.8 \times 10^{-11}$ erg cm^{-2} s^{-1}, as determined from its long term *RXTE* monitoring observations (Gliozzi et al. 2007). At a distance of 624 Mpc [1] this flux corresponds to an average luminosity of $\sim 5.6 \times 10^{44}$ erg s^{-1} during the *XMM-Newton* observations.

3.2. The iron line

The previous *XMM-Newton* data of PKS 0558-504 yielded low upper limits on the equivalent width of an iron line, either from neutral or ionised material (O'Brien et al. 2001; Brinkmann et al. 2004). The present data are consistent with the results from these

---

[1] This luminosity distance estimate is taken from NASA/NED. It is calculated assuming $H_0 = 73$ km s^{-1} Mpc^{-1}, $\Omega_{\mathrm{matter}} = 0.27$, and $\Omega_{\mathrm{vacuum}} = 0.73$.

Table 2. The iron-line best fit parameter values.

Obs.	E_{line} (keV)	$\Delta\chi^2$	EW (eV)
201	6.8	1.1 (175)	8 (<33)
301	6.69 ± 0.07	5.7 (188)	18 (<42)
401	6.95 ± 0.05	10.8 (276)	19 (<38)
501	6.90 ± 0.12	4.1 (251)	11 (<32)
601	6.83 ± 0.05	5.9 (264)	13 (<31)
Total	6.82 ± 0.10	22 (697)	23^{+25}_{-22}
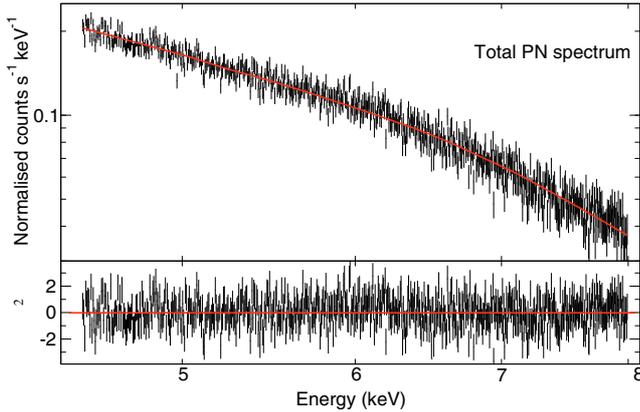
Fig. 3. *Top panel*: the best power law model fit to the total PN spectrum in the 4.5–8 keV band. *Lower panel*: the best-fit residuals plot.

studies: the best PL fit residuals to the individual spectra of the five observations do not show clear evidence for the presence of an iron line.

To investigate this issue in a more quantitative way, we refitted the five average spectra of each observation with the PL model in the 4.5–8 keV band. We fixed the best-fit spectral slope and then added a narrow Gaussian component to the model (the line width was kept fixed at a value of $\sigma = 10^{-5}$ eV). The best-fit results are listed in Table 2. The third column in this table lists the improvement in the best-fit χ^2 (i.e. $\Delta\chi^2$) when we added the Gaussian component to the model. The numbers in the parentheses indicate the degrees of freedom in the case of the PL model; the addition of the Gaussian component reduces this number by 2. The small $\Delta\chi^2$ values suggest that the addition of the Gaussian component is not statistically significant (except perhaps in the case of obs-401). The numbers in the parenthesis in the fourth column indicate the 90% upper limits on the equivalent width (EW) of the line. In fact, the best-fit E_{line} values turned out to be close to the starting values we chose. The rather low 90% upper limits imply that if there is an iron line in the energy spectrum of PKS 0558-504, it is weak.

For that reason, we combined the data from all orbits into a single spectrum and fitted it again with a power law model in the 4.5 to 8 keV energy range. Figure 3 shows the best power law model fit to the data, together with the residuals plot. The reduced χ^2 value of 767/697 d.o.f. implies a null hypothesis probability of 3.4%. The residuals indicate a low-amplitude excess emission around ∼6 keV. As before, we added a Gaussian component to the model and repeated the fit (keeping the best-fit spectral slope fixed). In this case, we also let the line's width, σ, be a free parameter. The best-fit results are also listed in Table 2 (the best-fit σ value was $0.19^{+0.24}_{-0.09}$ keV). The line's best-fit energy

is indicative of emission from Fe XXV. However, the large error of the line's equivalent width measurement suggests that the detection of the line itself is only at the 90% significance level. We therefore conclude that if there is an iron line in the spectrum of the source it is very weak ($EW \sim 20$ eV), and an indication of emission from ionized material.

3.3. The full band EPIC-PN spectrum

An extrapolation of the hard power law to low energies shows a clear "excess" of flux below ∼2 keV. This is demonstrated in Fig. 4. In the top panel we show the spectra of all observations. For demonstration reasons, the obs-601 and obs-501 spectra are multiplied by 1.5, while the obs-201 spectrum has been divided by 1.5. In this way, the spectra plotted from bottom to top correspond to the data from obs-201 to obs-601, in increasing order. The spectra have been fitted with a PL model in the 2–10 keV band (the solid line in the same panel indicates the best PL model fit to the obs-201, hard band spectrum). The bottom panel in Fig. 4 shows the "data over the best hard band PL fit" ratio. It is difficult to spot the data for the individual observations at energies higher than 2 keV in this panel, because the PL model fits all spectra well at these energies. As a result the data/model ratio is close to unity in all of them. However, at energies below ∼2 keV, a strong, featureless excess on top of the extrapolation of the 2–10 keV PL fit is clearly evident. The soft excess is almost 1.5–2 times "stronger" than the extrapolation of the hard band power law continuum. Interestingly, the data plotted in the lower panel of Fig. 4 indicate that the amplitude of this excess emission is variable.

Various models have been proposed for the "soft excess" component in NLS1 galaxies. In PKS 0558-504 in particular, O'Brien et al. (2001) fitted three black body components to this excess, Brinkmann et al. (2004) used an extra Comptonisation component, while Haba et al. (2008) used a multicolour disc black body model. Finally, recent claims about the connection of strong radio loud NLS1 galaxies with BL Lac objects (Yuan et al. 2008) raise the possibility that the X-ray spectra in objects like PKS 0558-504 could be modelled by broken power laws.

To check which of the proposed models provides the best interpretation of the source's X-ray spectrum, we fitted the spectra from the five individual observations with various models. In Fig. 5 we show the data-to-model ratios for fits of four different models. The fits were performed in the 0.4–10 keV band, by keeping the PL spectral slopes fixed at the values listed in Table 1.

In the top panel of Fig. 5 we show the data-to-model ratio when we used a bremsstrahlung component to account for the soft excess ("PLBrems" hereafter, for the combination of a "hard power law plus a bremsstrahlung component"). The residuals are similar in all five spectra (for this reason it is difficult to spot the residuals for the individual spectra in this panel). The best-fit resulted in a χ^2 of 5796 for 5203 d.o.f. and is formally not acceptable. The residuals show small amplitude absorption structures near the OI edge and perhaps near ∼0.7 keV as well (observers frame).

In the following panel we present the data-to-model ratio plot for the case for which we fitted the full band spectrum with a broken PL model ("BKNPL", hereafter). For clarity reasons, we plot the data-to-model ratio only for the obs-201 spectrum in this panel as well as the remaining panels of Fig. 5. The model residuals are almost identical for the other spectra as well. We found
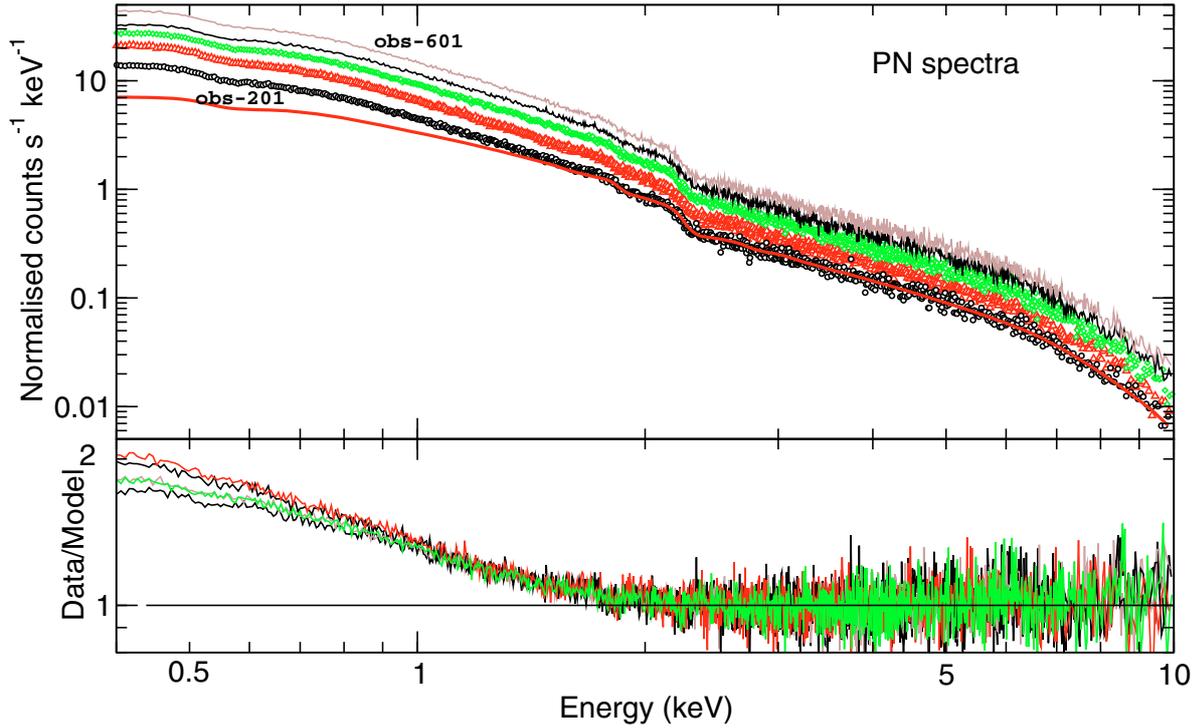
Fig. 4. *Top panel*: the 0.4–10 keV PN spectra of all observations. Black, open circles indicate the obs-201 spectrum; red, open triangles indicate the obs-301 spectrum, and green, open diamonds indicate the obs-401 spectrum. The obs-501 and obs-601 spectra are plotted with a continuous black and brown line. Some of the spectra are scaled for demonstration reasons (see text for details). The solid line indicates the best PL fit to the obs-201, 2–10 keV spectrum. *Lower panel*: the "Data/the best hard band PL model fit" plots for the same spectra (plotted using the same colour code as in the top panel).

that the fit was slightly worse in this case (χ^2 = 6196/5203 d.o.f.). The best-fit soft band slope and break energy were varying between 2.5 and 2.7, and 1.8–2 keV, respectively.

In the bottom two panels, we show the data-to-model ratios when we used two "physical" models, namely the `compTT` and `DISKBB` models in `XSPEC`, to account for the soft excess. In the case of the `compTT+PL` model (χ^2 = 6863/5293 d.o.f.), we first fitted the spectra by letting T_0 free to vary. The resulting best-fit values were similar for the five spectra, and for this reason we repeated the fit by forcing T_0 to be the same in all cases. The best fit T_0 value turned out to be ~0.14 keV, while kT, and τ were varying between ~2–4.4 keV and ~1.5–2.6, respectively. In the case of the `DISKBB+PL` model (χ^2 = 8024/5203 d.o.f.), the best-fit temperature at the inner radius was ~0.16–0.18 keV. We also tried models like a combination of two power laws, or a black body plus a hard band PL, but these models resulted in significantly worse fits.

The amplitude of the residuals becomes larger at energies below 0.4 keV. Using the whole energy band, i.e. ≥0.2 keV, yielded much larger best fit χ^2_{red} values. This indicates either a failure of the models at the lowest energies, or an inherent detector calibration uncertainty. To check the possibility of calibration uncertainties, we additionally performed fits (using the PLBrems model) with the single events (PATTERN = 0) of the PN and with the MOS1 data. Open circles, open squares and the filled diamonds in Fig. 6 indicate the 0.25–10 keV best-fit data-to-model residuals in the case of obs-601 for the MOS1, the single, and the single+double PN events spectra, respectively (we obtained similar results for the PN and MOS1 spectra of the other observations as well). The residuals for the single and single+double PN spectra are quite similar. On the other hand, there are differences between the PN and the MOS1 residuals below ~0.6 keV. At energies <0.4 keV, the MOS1 and PN residuals are quite

different. Their max-to-min difference is of the order of ~10%, a result which indicates that there exist unresolved detector calibration uncertainties at these low energies (it is for this reason that we considered the PN spectra at energies above 0.4 keV).

At higher energies, the difference between the MOS1 and the PN spectra is less than ~5% except for the 0.5–0.6 keV band (where we expect the instrumental and the Galactic oxygen edges to appear). This result implies that any "dips" in the residual plots at these energies (like the ones shown in Fig. 5) may be due to additional calibration uncertainties. Furthermore, the `compTT+PL` and `DISKBB+PL` residual plots in Fig. 5 exhibit a further shallow flux deficit around ~0.7 keV, which may correspond to low amplitude absorption features intrinsic to the source. This possibility can be investigated with the study of the RGS spectrum, which we describe below.

3.4. The RGS data

We used the fitting package *Sherpa*, of the Chandra Interactive Analysis of Observation (*Ciao*) software (vs. 4.1.2), to simultaneously fit the total RGS1 and RGS2 spectra of PKS 0558-504. Both the RGS1 and RGS2 spectra are grouped at a resolution of 20 mÅ (~0.5 eV at 0.5 keV), thus allowing for three bins for a RGS resolution element. For both the RGS1 and the RGS2 the photon count rate of the background spectrum becomes comparable to the background-subtracted source count rate at $E \lesssim 0.4$ keV ($\lambda \geq 30$ Å), and $E \gtrsim 2$ keV ($\lambda \leq 6.2$ Å). Moreover, due to failures of two different read-out detector chips early in the mission, both the RGS1 and the RGS2 lack response in two different spectral intervals: ~0.9–1.2 keV (RGS1) and ~0.5–0.7 keV (RGS2). Finally, a visual inspection of the RGS2 spectrum and its effective area revealed several regions where the
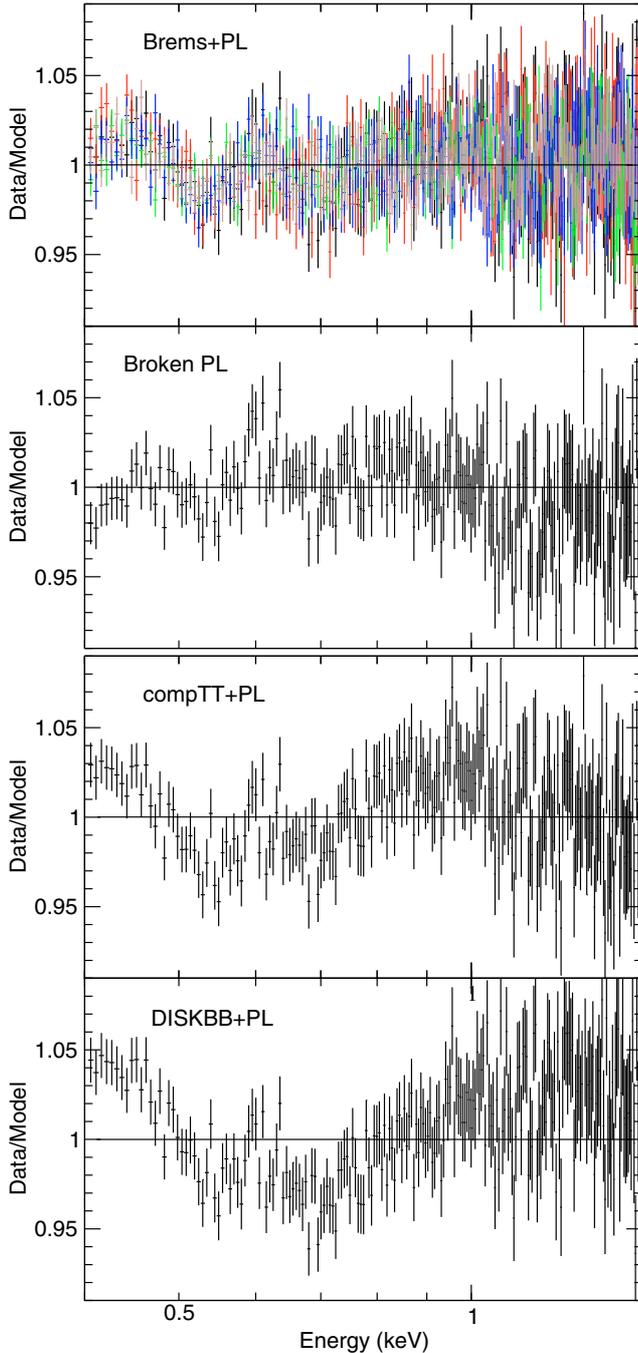
Fig. 6. "Data-to-PLBrems model" ratio in the 0.25−2 keV band, for the single PN events (open squares), single plus double PN events (filled circles), and the MOS1 spectra (open circles) of obs-601.

Fig. 5. *From top to bottom*: data-to-model ratio in the 0.4−2 keV band for the best fits of a Brems+PL, a broken PL, a `compTT`+PL, and a `DISKBB`+PL model. In the top panel, we plot the data for the the average spectrum of each *XMM-Newton* observation (black, red, green, blue and brown points have been used for the obs-201, obs-301, obs-401, obs-501, and obs-601 spectra, respectively). For clarity reasons, in the following panels, we plot the data for the obs-201 spectrum only (the data-to-model ratios are very similar for the other spectra as well).

Fig. 7. RGS1 (*top panel*) and RGS2 (*bottom panel*) residuals to a broken power law fit attenuated by Galactic absorption. For clarity reasons, the data in this figure are binned by a factor of 8 when compared to the unbinned RGS pipeline data. Consequently, the spectra plotted in this figure are grouped at about 40 Å per resolution element, i.e. at about 1.5 bins per RGS resolution element.

modelling of effective area features failed to properly reproduce the data. These were mostly concentrated at $E \lesssim 0.5$ keV and in two narrow regions at $E \sim 0.84$ keV and $E \sim 1.08$ keV. We therefore considered the following two RGS1 and RGS2 spectral intervals for spectral fitting purpose: (0.4−0.9) + (1.2−2)] keV and (0.69−0.82) + (0.85−1.07) + (1.09−2)] keV, respectively.

Due to the EPIC-RGS cross calibration problems, the RGS data cannot be compared directly to the PN best-fit models.
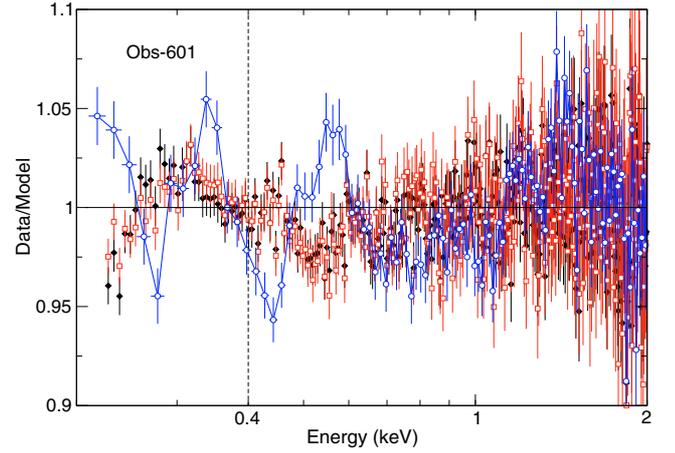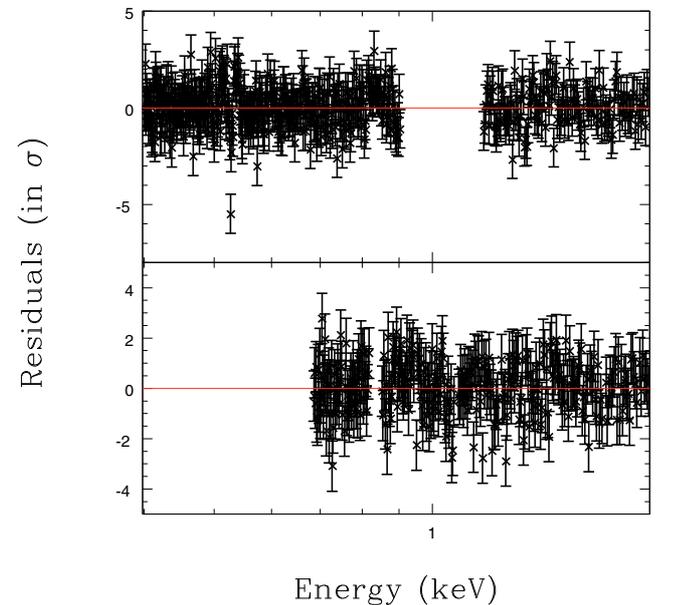
However, this is not a serious problem, as our main aim in this work is to identify any strong emission and/or absorption features in the RGS spectra that should be included in the models we use to fit the PN spectra. To this end, all we need is to model the continuum in the RGS spectrum as accurately as possible and search for any remaining residuals.

We first fitted a simple power law attenuated by neutral absorption, set to be at least equal to the Galactic column along the line of sight. Although the fit is statistically acceptable, $\chi^2 = 936.4/918$ d.o.f., a visual inspection of the broad band 0.4–2 keV residuals shows a flattening at energies higher than ~1.2 keV, both in the RGS1 and RGS2. We therefore replaced the PL with a broken power law model. This fitted the 0.4−2 keV continuum in the RGS spectra very well ($\chi^2 = 874.4/914$ d.o.f.). The best-fit residuals are shown in Fig. 7.

The residuals do not show any significant spectral features identifiable with either absorption or emission transitions within ± 5000 km s^{-1} from the systemic redshift of PKS 0558-504, that should be considered in the PN spectral fits. In particular there are no signatures of ionised material (i.e. the so-called "warm absorbers"; WA) which are observed in other Seyferts. We tried to investigate this in a more quantitative way by adding *PHASE*, i.e. the warm absorber model of Krongold et al. (2003), to the broken power law model. We fixed the turbulence velocity of the absorber to 200 km s^{-1} (unresolved in the RGS), and left the ionisation parameter U (defined as the ratio between the photon volume density at the location of the absorbing cloud and the electron density in the cloud) and the equivalent column density of the absorber, $N_{\rm H}$, free to vary. The redshift of the absorber was fixed to the systemic redshift of PKS 0558-504, and its outflow/inflow velocity was allowed to vary between -5000 km s^{-1} and $+5000$ km s^{-1}.

The best model fit was achieved for $\log(N_{\rm H}) = 20$ (the lowest tabulated value in the model) and $\log(U) = 1.37$. At these column densities and for this ionisation parameter, the gas is already fully transparent in the RGS band. The best-fit parameter values are not well determined, but the allowed parameter values (for example $\log(U) > 2$ for $\log(N_{\rm H}) = 20$–21, and $\log(U) > 2.3$ if $\log(N_{\rm H}) = 21$–22) are incompatible with the parameter space which would be normally occupied by a WA (i.e. $\log(N_{\rm H}) = 20$–22 and $\log(U) < 1.1$–2). We therefore conclude that the presence of a warm absorber is not required by these data. A more detailed study of the RGS spectrum of the source is presented in Nicastro et al. (submitted to ApJ).

4. Spectral variability

The discussion in the above sections suggests that unaccounted detector calibration inaccuracies may be responsible for the $\sim$0.5–0.6 keV "dip" in the residual plots shown in Fig. 5. However, such inaccuracies most probably cannot explain the remaining residuals, such as the the "wavy" pattern we see in the two lower panels of the same figure for example. The absence of warm absorbing signatures cannot explain them either.

Before reaching conclusions regarding the quality of the model fits to the average spectra of each observation, we have to consider the fact that, as shown in Fig. 1, the source exhibits continuous, large amplitude flux variations on both short and long time scales. If these flux variations are associated with spectral variations as well (as it is usually the case in Seyfert galaxies), then model fitting of some kind of "average" spectrum may yield dubious results.

To illustrate the presence of spectral variations during the *XMM-Newton* observations, we estimated the ratio of the 2–10 keV over the 0.4–1 keV count rates (i.e. the "hardness ratio", or simply HR), using light curves binned in 100 and 1000 s. The top panel in Fig. 8 shows the HR values for the obs-601. The respective light curve is plotted in the lower panel. The first result from this plot is that the HR does not stay constant, i.e., the source exhibits significant spectral variations, although of an amplitude smaller than that of the flux variations: the max-to-min ratio for the HR values is $\sim$1.4, as opposed to $\sim$3.3 for that of the observed count rates.

There is also an indication that the spectral variations are anti-correlated with the flux variations. For example, approximately 7–20 ks after the start of obs-601 the flux increases while HR decreases, and in the next 20 ks HR increased while the total source flux decreased. This "HR–flux" anti-correlation is not "perfect" though. For example, around 95–105 ks after the start
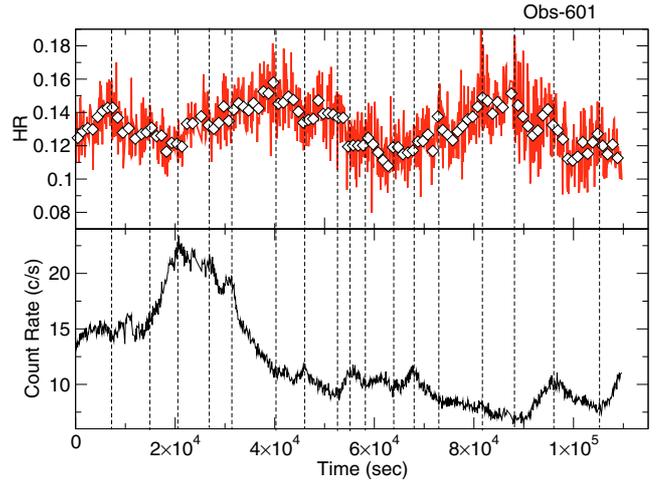

Fig. 8. *Top panel*: HR plotted as a function of time (obs-601). Points shown in grey indicate the HR using bins of the size of 100 s, while open diamonds indicate the HR values using bins of the size of 1000 s (for clarity reasons errors in the latter case are not plotted; they are of the order of $\sim$5 × 10^{-3}). *Lower panel*: the full band light curve (using bins of the size of 100 s). The vertical dashed lines indicate the observation segments we used for the time resolved spectroscopy (see text in Sect. 5 for details).

of the observation, HR is positively correlated with the source flux: they both decrease with time. A similar behaviour (i.e. significant HR variations, which are mainly anti-correlated with flux) is seen in the other observations as well (a detailed study of the spectral variability of the source with the use of HR plots, together with a cross-correlation analysis, will be presented in a forthcoming paper).

5. Time resolved spectroscopy

To study the spectral variability of the source, we split up obs-201, 301, 401, 501 and 601 in 11, 12, 20, 17 and 18 (78 in total) individual data stretches. This was done in a way that the segments would broadly correspond to either a flux-rising or flux-decaying phase. The vertical lines in Fig. 8 indicate the individual segments that we considered in the case of obs-601. The shortest and longest exposures of a segment in all observations are 2 ks and 20 ks, respectively. As the count rate of the source is sufficiently large, each of the individual spectra had more than several ten thousand photons in the 0.4–10 keV band. This is sufficient for an accurate determination of the parameters of the relatively simple spectral model we used to fit them. Our objectives were to use a simple model to correctly parametrise the shape of each one of these spectra, and determine the best-fit parameter values to investigate whether (and how) the hard and soft band spectra vary in flux *and* shape.

Regarding the hard band (i.e. 2–10 keV) spectra, a PL model fitted them well. However, it does not provide an acceptable fit to the 0.4–2 keV band as well. A soft excess emission component was almost always present at energies below $\sim$2 keV. We therefore used the PLBrems model to fit the full band spectra. The model fit was first performed in the 2–10 keV band. We then kept the PL slope and normalisation fixed at their best-fit values when we fit the full band spectrum.

The quality of this model fit was statistically acceptable in all cases: the mean reduced χ^2 of all 78 fitted spectra is $\langle \chi^2_{\rm red} \rangle = 0.991$, with a standard deviation of $\sigma = 0.006$. Figure 9 shows one of the worst PLBrems fits ($\chi^2_{\rm red} = 1.068/821$ d.o.f.); the
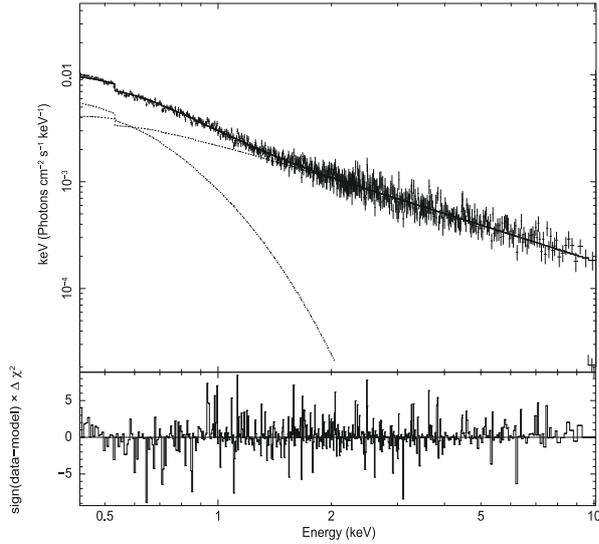
Fig. 9. Plot of one of the worst PLBrems fits (*top panel*), and of the respective residuals (*bottom panel*) to the PN data of one of the individual spectra (see Sect. 5 for details).

Fig. 10. The "total" model flux (i.e. $Flux_{PL/2-10\,keV}+Flux_{PL/0.4-1\,keV}+Flux_{Brems}$) plotted as a function of the observed 0.4–10 keV count rate.

data shown correspond to the time interval between ~51−70 ks after the start of obs-301. The dotted lines in the top panel of this figure indicate the PL component ($\Gamma \sim 2.12$) and the bremsstrahlung emission of ~0.16 keV which best fitted the spectrum. In the bottom panel we show the contribution to the total χ^2 per spectral bin. The residuals plot does not indicate any systematic large amplitude deviations between the data and the best-fit model. We reached a similar conclusion when we investigated the residual plots for all the other spectra as well.

Although bremsstrahlung emission cannot account for the soft excess emission in PKS 0558-504 (if that were the case we would expect to detect a plethora of emission lines in the RGS spectrum of the source) our results indicate that this model can adequately parametrise the shape of this component. We therefore decided to use the PLBrems best-fit results to study the spectral variability properties of the source. In particular, we used the best PL spectral slope, Γ, as a representation of the hard band spectral shape, and the (un-absorbed) 2–10 keV and 0.4–1 keV PL flux ($Flux_{PL/2-10\,keV}$ and $Flux_{PL/0.4-1\,keV}$) as a measure of the power law continuum flux in the hard and soft bands, respectively. We also used the (un-absorbed) 0.4–1 keV flux of the bremsstrahlung spectral component ($Flux_{Brems}$) as a representative of the soft excess flux in this object (i.e. of the flux of the excess emission on top of the hard band PL component, which is assumed to extend down to ~0.4 keV with the same slope), and the Brems temperature, kT, as a representative of the soft excess shape.

As a simple "sanity" check that our model-fitting results agree with the observed variations, Fig. 10 shows the "total" model flux (i.e. the sum of $Flux_{PL/2-10\,keV}$, $Flux_{PL/0.4-1\,keV}$ and $Flux_{Brems}$) plotted as a function of the mean, 0.4–10 keV count rate of each segment. The expected one-to-one relation between these two quantities is obvious from this plot.

5.1. The hard band spectral variability results

The top panel in Fig. 11 displays Γ as a function of time measured from the start of the *XMM-Newton* observations. The power law spectral slope is significantly variable; we find that $\chi^2 = 593/77$ d.o.f., when we fit a constant to the "Γ vs time"
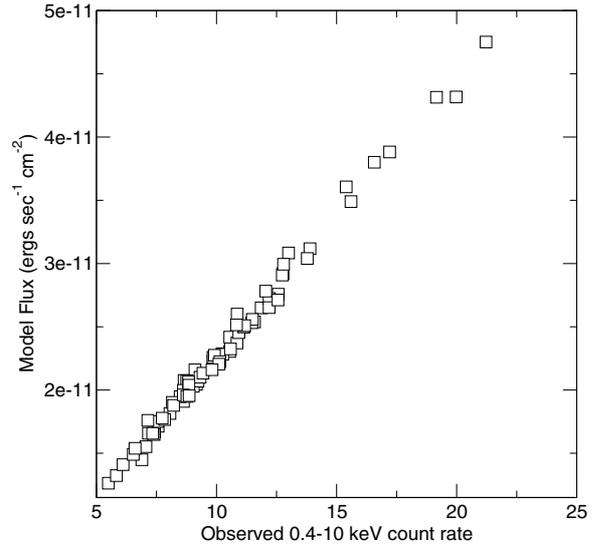
plot. The average spectral slope is $\overline{\Gamma} = 2.152 \pm 0.001$. The individual spectral slopes vary between ~2−2.3, which implies a max-to-min variability amplitude of 15%. The fractional root mean square variability amplitude (corrected for the experimental noise) of the spectral slope variations is $f_{rms,\Gamma} = 3.8 \pm 0.1\%$[2]. The small amplitude Γ variations indicate that the observed count rate variability is mainly caused by variations of the PL normalisation. Figure 12 shows that this is indeed the case.

Filled and open circles in the lower panel of Fig. 11 indicate $Flux_{PL/2-10\,keV}$ and $Flux_{PL/0.4-1\,keV}$. A comparison between the top and bottom panels shows that the spectral slope and flux variations are highly correlated: the spectrum becomes steeper with increasing flux. This correlation became clearer when we plotted Γ as a function of the observed 0.4−10 keV count rate (top panel in Fig. 13). This is the first time that such a positive spectral-flux variability correlation (which is commonly detected in other nearby Seyferts) is detected for this source.

Filled (open) triangles in the top panel of Fig. 13 indicate the spectral slope during the periods when the source flux increases (decreases), Γ_{up} (Γ_{down}). On average, the source spectrum appears to be steeper when the flux increases: $\overline{\Gamma}_{up} = 2.18 \pm 0.015$ and $\overline{\Gamma}_{down} = 2.14 \pm 0.015$. But this difference is not highly significant ($\Delta\overline{\Gamma} = 0.04 \pm 0.02$). The solid and dashed lines in the same panel indicate the best line fits to the (Γ_{up}, CR) and the (Γ_{down}, CR) data sets, respectively. The best-fit lines also imply that, on average, most of the time Γ_{up} is steeper than Γ_{down}, but the difference of the best-fit line parameters is not statistically significant. We therefore cannot rule out that the shape of the X-ray continuum varies with flux in a similar way, irrespective of whether the source flux increases or decreases.

5.2. The soft excess spectral variability results

Points plotted with crosses in the lower panel of Fig. 11 indicate $Flux_{Brems}$, plotted as a function of time. The average soft excess flux is $4.23 \pm 0.01 \times 10^{-12}\,\mathrm{erg\,cm^{-2}\,s^{-1}}$, which is smaller than the average PL flux in the same band ($\overline{Flux}_{PL/0.4-1\,keV} = 6.6 \times 10^{-12}\,\mathrm{erg\,cm^{-2}\,s^{-1}}$). Furthermore, the soft excess flux is

---

[2] The error, accounting only for the measurement error of Γ, has been calculated according to the prescription of Vaughan et al. (2003).
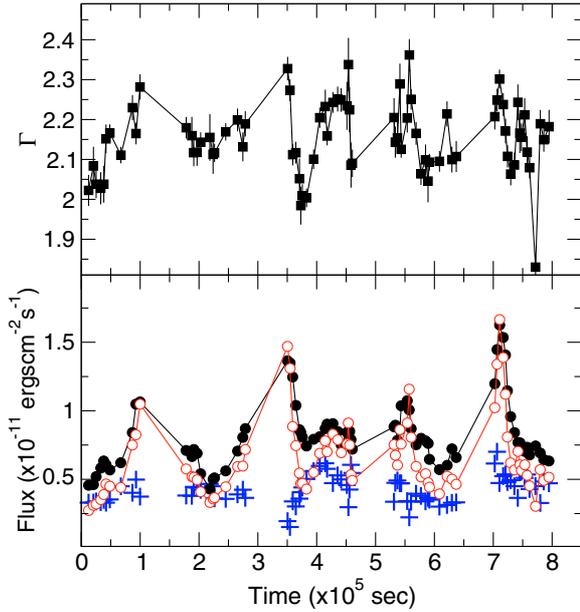
Fig. 11. *Top panel*: the best-fit spectral slope of the individual spectra of the source, plotted as a function of time (measured from the start of the *XMM-Newton* observations). *Lower panel*: filled, open, and crosses indicate $\text{Flux}_{\text{PL/2–10 keV}}$, $\text{Flux}_{\text{PL/0.4–1 keV}}$, and $\text{Flux}_{\text{Brems}}$, respectively.
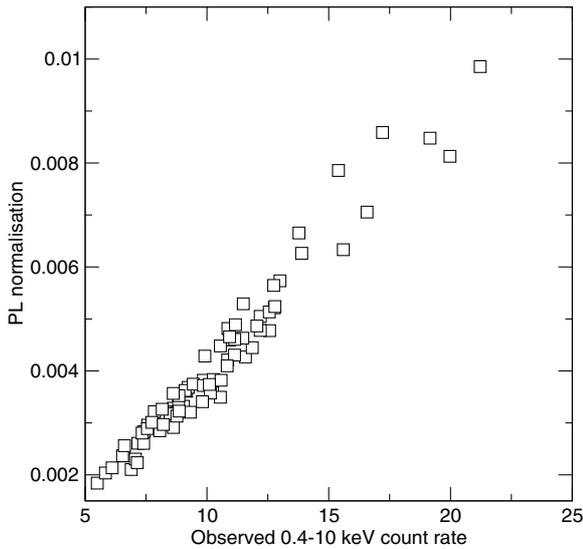

Fig. 12. The best PL model fit normalisation values plotted as a function of the observed 0.4–10 keV count rate.

significantly variable ($\chi^2 = 47361/77$ d.o.f.), but its average amplitude is smaller ($f_{\text{rms,Brems}} = 23.7 \pm 0.2\%$) than the average PL variability amplitude in the 0.4–1 keV band ($f_{\text{rms,PL/0.4–1 keV}} = 42.7 \pm 0.2\%$).

The shape of the soft excess is also variable. The best-fit kT values are not consistent with the hypothesis of a constant temperature ($\chi^2 = 1385/77$ d.o.f.). These variations are of a rather small amplitude ($f_{\text{rms,}kT} = 11.9 \pm 0.4\%$). Crosses in the bottom panel of Fig. 13 indicate the best-fit kT values plotted as function of CR. The soft excess shape appears to be broadly correlated with the source flux: the temperature increases with increasing flux. Application of the Kendall's τ test resulted in a value of $\tau = 0.33$, which implies a rather weak, but significant, correlation between kT and the source flux (the probability of the null hypothesis is less than 3×10^{-5}). We conclude that as the source
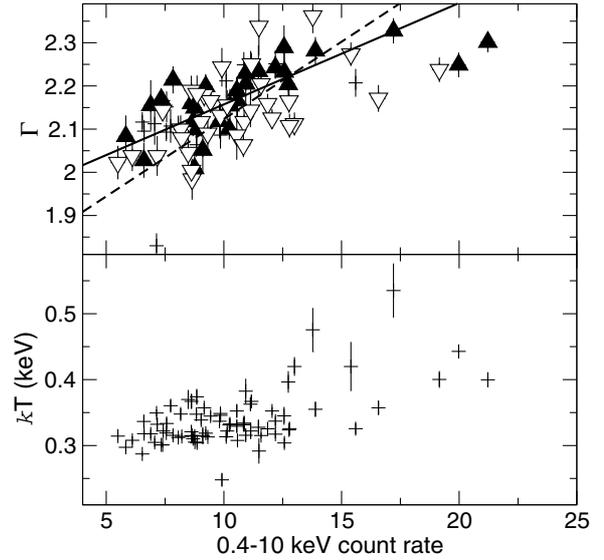

Fig. 13. *Top panel*: the best-fit spectral slope of the individual spectra of the source, plotted as the function of the 0.4–10 keV count rate. Filled "up-triangles" and open "down-triangles" indicate the Γ_{up} and Γ_{down} values, while the solid and dashed lines are the best line fits to these data sets. *Lower panel*: the best-fit Brems kT values for the individual spectra of the source, plotted as the function of the 0.4–10 keV count rate.

flux increases kT increases as well, i.e. the soft excess "shifts" to higher energies. The average kT is 0.34 ± 0.01 keV, which remains the same irrespective of whether the flux is increasing or decreasing. The best line fits to the (kT_{up}, CR) and the (kT_{down}, CR) data sets are also almost identical. We therefore conclude that the shape of the soft excess varies with flux in a similar way, irrespective of whether the source flux increases or decreases.

5.3. Cross-correlation between soft excess and hard power law flux

The bottom panel in Fig. 11 indicates that the PL and Brems flux light curves are not highly correlated. To investigate this issue further, we split up all five observations in segments of 2000 s long (278 in total) and fitted their 0.4–10 keV band spectra with the PLBrems model. As above, the 2–10 keV band was first fitted with a PL model, and we kept the best-fit Γ and PL normalisation values fixed when we added the Brems component to fit the full band spectra. The model fitted all spectra well, and using the best-fit model parameter values we calculated $\text{Flux}_{\text{PL/2–10 keV}}$, $\text{Flux}_{\text{PL/0.4–1 keV}}$, and $\text{Flux}_{\text{Brems}}$.

We determined the cross-correlation between the PL and Brems flux light curves using the "Discrete Correlation Function" (DCF) method of Edelson & Krolik (1988). The DCF was calculated using lags of size 2000 s and in a way that a significant correlation at positive lags will indicate that the Flux_{PL} variations are leading those in the $\text{Flux}_{\text{Brems}}$ light curve. The results are plotted in the top panel of Fig. 14, in the case of the DCF between the $\text{Flux}_{\text{PL/0.4–1 keV}}$ and $\text{Flux}_{\text{Brems}}$. The maximum DCF amplitude reaches a value of $\text{DCF}_{\text{max}} \sim 0.6$ at a lag of $\text{lag}_{\text{max}} \sim -20$ ks (the results are similar when we cross-correlated $\text{Flux}_{\text{PL/2–10 keV}}$ and $\text{Flux}_{\text{Brems}}$, except that $\text{DCF}_{\text{max}} \sim 0.5$ in this case).

The DCF_{max} value of ~ 0.6 implies that the hard band continuum and the soft excess flux variations are weakly correlated. The bottom panel in Fig. 14 shows the $\text{Flux}_{\text{PL/0.4–1 keV}}$ and $\text{Flux}_{\text{Brems}}$ light curves (open squares and grey continuous line,
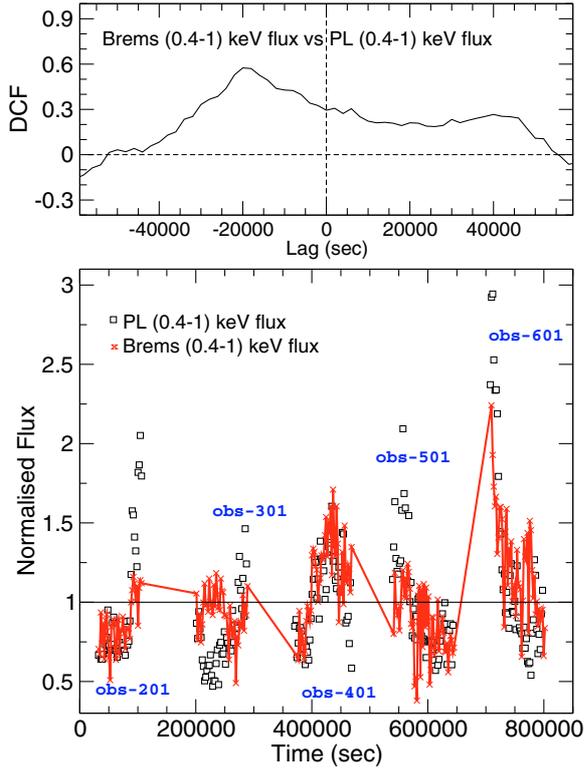
Fig. 14. *Top panel*: the DCF between $Flux_{PL/0.4-1\,keV}$ and $Flux_{Brems}$. *Bottom panel*: the respective light curves (open squares and crosses, respectively), normalized to their mean. The soft excess light curve has been shifted by +20 ks, and we plot only the light curve parts which overlap.

respectively), normalised to their mean. The soft excess light curve is shifted by +20 ks, and we have plotted only these parts of the light curves which overlap (i.e., those light curve parts which correspond to the estimation DCF at lag = -20 ks). This plot clarifies why the correlation between the hard band continuum and the soft excess variations is just moderate. The observed variations agree reasonably well during obs-401, 501 and 601. But the soft and hard band fluxes are not correlated during obs-301, while the situation is unclear for obs-201. Furthermore, the difference in the variability amplitude (even in those cases when the correlation is reasonably good) contributes to the decrease in the DCF_{max} amplitude. In any case, even if the two light curves are indeed intrinsically correlated, the negative time lag implies that it is the soft excess flux variations which *lead* the hard band continuum variations.

6. The full band PN spectrum revisited

Given the complex spectral variability of the source, we chose seven of the 78 segments into which we originally split the total *XMM-Newton* observation, based on the following criteria: i) HR remained constant during the exposure of each segment, ii) the average count rate is different and adequately samples the observed flux variability amplitude of the source, and iii) there are enough photons in the spectra to ensure a sufficiently high signal to noise ratio. The first and second columns in Table 3 list the start time, the exposure time, and the average count rate of the segments we chose (segments are listed in a decreasing order of the average count rate). There are more than $\sim$60 000 photons in the 0.4–10 keV band of each one of these spectra.
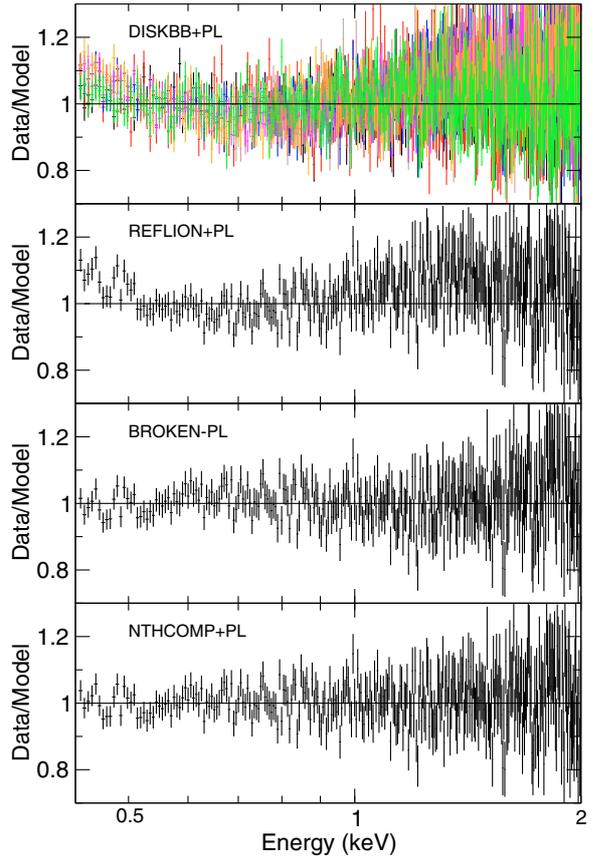
Fig. 15. *From top to bottom*: data-to-model ratio in the 0.4–2 keV band for the best fits of a `DISKBB+PL`, `REFLION+PL`, a broken PL, and a `NTHCOMP+PL` model to the seven individual spectra we considered in Sect. 6. The residuals for the spectra listed in Table 3 are plotted with points in black, red, green, blue, brown, magenta and orange, respectively. It is difficult to identify the individual residual plots for each spectrum, because they are similar for all of them. For clarity reasons, in the following panels we plot the best-fit residuals in the case of the spectrum of the fourth segment listed in Table 3 only. The residuals are similar for the other spectra as well.

First, we fitted the 2–10 keV spectrum of each segment with a PL model (best-fit slopes, Γ_{hard}, are listed in the third column of Table 3), which fitted the high energy part of the spectra well. Then we kept Γ_{hard} and the best-fit PL normalisation fixed, and we fitted the 0.4–10 keV spectra with the following more physically motivated additional models:

a) a standard accretion disc, multi black body spectrum, i.e. `DISKBB`. The best-fit temperature at the inner disc radius, T_{in}, turned out to be similar in all cases. We therefore re-fitted the spectra simultaneously by keeping T_{in} the same for all seven spectra. The model gave a poor fit to the data ($\chi^2 = 6027/5122$ d.o.f.). The best-fit residuals are plotted in the top panel of Fig. 15. They are plotted with points in black, red, green, blue, brown, magenta and orange for the spectra as listed in Table 3. They are very similar for all spectra, and for that reason it is difficult to spot the residuals for each spectrum in this panel;

b) a relativistically blurred photo-ionised reflection model. We used the model of Ross & Fabian (2005) (which is available as an additional table model, `REFLION`, in XSPEC), in which a semi-infinite slab of optically thick cold gas of a constant density is illuminated by a PL continuum. Although we did not detect any significant evidence for disc reflection in the

Table 3. Results from the spectral fits of the `NTHCOMP`+PL model to the 0.4–10 keV spectra of the seven short segments (see section 6 for details), assuming the same electron temperature ($kT = 0.42 \pm 0.01$ keV), and disc-black body seed photon temperature ($kT_{bb} = 0.11^{+0.004}_{-0.01}$ keV), in all cases.

Time day/UT	Exp. / $\overline{CR}$ ks / (c/s)	Γ_{hard}	Γ_{Comp}
2008-09-15; 05:33:50	4.2/19.98	2.26 ± 0.05	2.68 ± 0.07
2008-09-15; 04:30:23	3.8/15.60	2.21 ± 0.05	3.31 ± 0.11
2008-09-08; 02:59:53	6.8/12.77	2.21 ± 0.04	3.65 ± 0.15
2008-09-11; 21:22:40	9.8/11.86	2.10 ± 0.04	3.10 ± 0.06
2008-09-11; 11:39:12	12/8.62	1.95 ± 0.04	3.22 ± 0.06
2008-09-09; 21:28:49	20/7.34	2.05 ± 0.04	3.08 ± 0.05
2008-09-14; 04:22:24	12.9/6.60	2.01 ± 0.04	3.05 ± 0.06

Notes. Columns 1 and 2 list details of the segments we used.

hard band spectrum of the source, we considered this model, because strong blurring effects from the relativistic accretion disc can smear the iron line almost completely and at the same time result in a featureless soft excess emission. For each spectrum, we kept the PL continuum slope fixed at the Γ_{hard} values listed in Table 3, and we added the illuminating and reflected components (with the amount of each free to vary). To simulate the blurring from the disc, we convolved the total emission with a Laor (1991) line profile (`KDBLUR` model in `XSPEC`). We fitted the seven spectra simultaneously, with the same iron abundance of the disc (relative to solar). We also fixed the inner radius of the Laor profile to be 1.235 gravitational radii (the smallest radius allowed in the case of a maximally rotating BH), and we also assumed a common emissivity profile and the disc's inclination angle. The best-fit values were: emissivity index ~10 (which is the maximum value allowed in `KDBLUR`), inclination ~72 degrees, and iron abundance ~1.8. The ionization parameter of the gas was decreasing from $\xi \sim 3750$ to $\xi \sim 500$ for the highest to the lowest flux spectrum, respectively. The final best model fit was very poor ($\chi^2 = 7316.4/5119$ d.o.f.). In the second panel of Fig. 15, we plot the best-fit residuals in the case of the spectrum of the fourth segment listed in Table 3 only. The residuals are similar for the other spectra as well, and for clarity reasons we do not plot them;

c) a BKNPL model. This model is frequently used to parametrise the X-ray spectra of BL Lac objects (see e.g. Brinkmann et al. 2005). The spectra were fitted simultaneously by keeping the hard band slope fixed at Γ_{hard}. The best-fit "break energy", E_{break}, turned out to be ~2 keV in all cases, except for the highest flux spectrum, where $E_{break} \sim 2.9$ keV. The best-fit slope at soft energies was decreasing form ~2.7 to ~2.5, from the low to the high flux spectra. The best model fit is statistically acceptable in this case ($\chi^2 = 5081/5115$ d.o.f.). The data plotted in the third panel of Fig. 15 indicate the best-fit residuals in the case of the spectrum of the fourth segment listed in Table 3. The residuals have a similar shape and amplitude in the other spectra as well;

d) a low-temperature Comptonisation model. We first fitted the spectra individually, using the `compTT` model. The best-fit T_0 and τ values turned out to be quite similar for all spectra. For that reason, we re-fitted the spectra simultaneously, assuming the same T_0 and τ. The resulting best-fit electron temperature values were increasing from $kT \sim 2.8$ keV, in the

case of the largest flux spectrum, to ~5.4 keV, for the lowest flux spectrum. The fit was statistically acceptable, with a χ^2 value of 5124 for 5120 d.o.f. However, the best-fit residuals plot was qualitatively similar to the `compTT`+PL model residuals plotted in Fig. 5: they had a similar "wavy" pattern, with a deficit around 0.5–0.7 keV, although of significantly smaller amplitude.

To further investigate the issue of low-temperature Comptonisation, we also considered the model `NTHCOMP` in `XSPEC` (Zycki et al. 1999), which also describes the continuum shape from thermal Comptonisation. The parameters of the model are: a) the seed photon temperature, kT_{bb}, b) the electron temperature, kT_e, and c) the asymptotic power law photon index, Γ_{Comp} (which is set by the combination of the electron scattering optical depth and kT_e). We first fitted the seven spectra separately (assuming a disc-black body soft photon input). We noticed that the individual best-fit kT_{bb} and kT_e values were similar. We therefore re-fitted the spectra simultaneously, assuming the same kT_{bb} and kT_e. The model fit was very good, with a χ^2 of 4997 for 5120 d.o.f. (the best-fit residuals plot shown in the bottom panel of Fig. 15 is for the spectrum of the fourth segment listed in Table 3; similar residuals were observed for the other spectra as well). The best-fit electron and seed photon temperatures were $kT_e = 0.424 \pm 0.012$ keV and $kT_{bb} = 0.11^{+0.004}_{-0.01}$ keV. The best-fit Γ_{Comp} values for this model are listed in Table 3.

Both the BKNPL and the `NTHCOMP`+PL models gave a good fit to the data. However, in the case of the latter model, we got a reduction in the best-fit χ^2 value of $\Delta\chi^2 = 84$ with a *smaller* number of model parameters. Following Mushotzky (1982), we defined the ratio of the likelihood of the best BKNPL fit, L_{BKNPL}, to the likelihood of the best `NTHCOMP`+PL model fit, L_{Comp}, as: $L_{BKNPL}/L_{Comp} = \exp[(\chi^2_{BKNPL} - \chi^2_{Compt})/2] = \exp(\Delta\chi^2/2) \sim 2 \times 10^{18}$, in our case. This high value strongly suggests that the Comptonisation model is much more likely than the BKNPL model to be the "correct" model for the soft excess in PKS 0558-504.

7. Summary and discussion

We presented the results from the spectral analysis of a long *XMM-Newton* observation of the luminous, radio-loud, narrow line Seyfert 1 galaxy PKS 0558-504. The object was observed in September 2008 for 5 orbits, yielding data of unprecedented quality for this source. The main results from our work are summarised below:

1) The source exhibits continuous, large amplitude flux variations on all sampled time scales. A flux variability study with the use of the power spectrum analysis will be presented in a companion paper.
2) The 2–10 keV band spectrum of the source is well fitted by a simple PL model, with a steep slope of $\Gamma \sim 2.15$, which is typical of NLS1.
3) The hard band slope is variable; the spectrum steepens as the flux increases. This is similar to what is commonly observed in other Seyferts as well (see e.g. Sobolewska & Papadakis 2009).
4) The hard band spectrum is very smooth; we did not observe any absorption features (either lines or edges), and we found only weak evidence for the presence of an iron line, which is indicative of emission from highly ionised iron. The line's

EW is small, ~20 eV, with an 90% upper limit of no more than ~45–50 eV.

5) At energies below ~2 keV a strong, steep, smooth, and broad soft excess component appears. The soft excess flux is variable, but with an amplitude which is smaller than the hard band continuum variability amplitude. The soft excess spectra shape is also variable and becomes "harder" with increasing flux.

6) The soft excess and the hard band flux variations are moderately correlated, but with a delay: the former are leading the latter by ~20 ks.

7) We detected no signs of warm absorption features at energies below ~2 keV.

8) The average 0.4–10 keV spectra of the individual *XMM-Newton*, orbit-long observations cannot be fitted well by any of the models that are commonly used to fit similar data of other NLS1. This could be partly due to remaining uncertainties in the instrumental PN calibration. But we believe that the spectral variability of the source, and in particular the variable soft/hard flux ratio (even on time scales of the order of a few ks), significantly affects the the results from the spectral analysis of spectra which are averaged on time scales longer than 10–20 ks.

9) Model-fitting to the spectrum of a few short segments of the total observations showed that the soft excess can be well described by a low-temperature Comptonisation model of the disc photons, in agreement with the results of Brinkmann et al. (2004). Other alternatives like emission from a multicolour disc black body, or reflection from an ionised disc, could not fit the data well. A broken power law model also provided a statistically acceptable fit to the data, however, the low-temperature Comptonisation model is a more likely explanation of the source spectrum.

Although PKS 0558-504 is one of the few radio-loud NLS1, its X-ray spectrum seems to be "normal" and rather similar to the spectra of other NLS1. Our results rule out a jet origin for the bulk of the X-ray emission from this object: the hard band slope of ~2.15 is similar to the X-ray slope of most radio-quiet NLS1s, the "soften when brighter" spectral variability trend of the power law continuum is identical to what is observed in other radio-quiet Seyferts, and even the weakness of the iron line emission is also consistent with what is observed in other NLS1s. Furthermore, the fact that we found no evidence for ionised absorption in either the soft or the hard X-ray bands implies that the X-ray spectrum of PKS 0558-504 is essentially unmodified by intervening matter. As a result, the present data set is ideal to study the intrinsic, X-ray emission spectrum of this object, free from absorption effects. Given the similarity between the X-ray emission properties between PKS 0558-504 and other NLS1s, some of the results from the present study may have wider implications to NLS1 as a class.

However, PKS 0558-504 may still be a rather rare object, because it almost certainly has a high mass accretion rate, $\dot{m}$. To estimate this rate in Eddington units, $m_{\rm Edd}$, we need to know the mass of the BH in the nucleus of PKS 0558-504. We can estimate it by using the virial relation $M_{\rm BH} = R(\Delta V)^2/G$, where R and ΔV are the radius and velocity dispersion of the broad line region. We measured the velocity dispersion from the width of the broad Hβ emission line (Corbin 1997) and the radius of the broad line region from the radius–luminosity scaling relation of Bentz et al. (2009), using the 5100 Å luminosity measurement of Corbin & Smith (2000), and we found that $M_{\rm BH} \sim 5.8 \times 10^7 \, M_\odot$. The average 2–10 keV flux of ~1.8×10^{-11} erg cm^{-2} s^{-1}

(Gliozzi et al. 2007) implies an average 2–10 keV luminosity of ~8.4×10^{44} ergs/s, which is already ~11% of the Eddington luminosity ($L_{\rm Edd}$) for this BH. Even if we use the lowest bolometric correction of ~20 of Vasudevan & Fabian (2009), the bolometric accretion rate of the source turns out to be larger than the Eddington accretion rate, $\dot{m}_{\rm Edd}$. In fact, the combined analysis of the present data set with simultaneous SWIFT observations implies that the source is accreting at a rate which may be several times larger than $\dot{m}_{\rm Edd}$ (Gliozzi et al., in preparation). Keeping this fact in mind, we present below a discussion of some of the results we reported above.

The hard band X-ray spectral variability of PKS 0558-504. Despite the high accretion rate of the source, its hard band spectrum is not unusual. It has a power law shape, which, as we mentioned in Sect. 3.1, can be explained by thermal Comptonisation of seed photons by a hot electron corona whose parameters are similar to those which can also explain the hard band X-ray spectrum of most radio-quiet Seyferts.

In the case of thermal Comptonisation, the spectral slope Γ is determined by the so-called Compton amplification factor, $A = (L_{\rm diss} + L_{\rm s})/L_{\rm s}$, where $L_{\rm diss}$ is the power dissipated in the corona and $L_{\rm s}$ is the intercepted soft luminosity. Obviously, if A varies, then Γ should also change as well. According to Beloborodov (1999), $\Gamma \propto (A - 1)^{-b}$, where $b \approx 0.1$, if the energy of the input soft photons, $E_{\rm in}$, is of the order of a few eVs, and $b \approx 0.17$, if $E_{\rm in}$ is of the order of a few hundred eV.

The data plotted in the top panel of Fig. 11 can be well fitted by a power law model of the form: $\Gamma \propto {\rm X\text{-}ray}_{\rm flux}^{0.15 \pm 0.02}$ (here X-ray$_{\rm flux}$ stands for the observed 0.4–10 keV count rate). A possible explanation then for the "spectral slope – X-ray flux" correlation is that the "heating-to-cooling" ratio of the corona, $(L_{\rm diss}/L_{\rm s})$, decreases with increasing X-ray flux (or accretion rate, if the X-ray flux is indicative of the accretion rate of the source), i.e. $(L_{\rm diss}/L_{\rm s}) \propto {\rm X\text{-}ray}_{\rm flux}^{-1}$. In this case, we would expect that $\Gamma \propto {\rm X\text{-}ray}_{\rm flux}^{b}$, with $b \approx 0.17$ in the case when the energy of the input photons is of the order of a hundred eV or so, exactly as observed.

The hard band spectral variations in PKS 0558-504 could also be explained by a combination of a highly variable (in flux) power law continuum (with a fixed slope) and a constant reflection component (e.g. Taylor et al. 2003; Ponti et al. 2006; Miniutti et al. 2007), or by variations in the column density, covering fraction, and/or the opacity of an absorber, while the continuum slope remains constant (e.g. Miller et al. 2008; Turner et al. 2007). Still, our results indicate that the X-ray spectrum of PKS 0558-504 is not modified by intervening absorbing material, while the failure of the reflection model to account well for the full band spectrum of the source (in various flux levels) implies that the reflection component is probably minimal in the 2–10 keV band (when compared to the PL continuum). For these reasons, we believe that the observed spectral variations in this source indicate *intrinsic* Γ variations. The fact that the "steeper when brighter" variability pattern of PKS 0558-504 is similar to what is observed in many Seyfert galaxies suggests that intrinsic Γ variations may also be responsible to a large extend for the spectral variations we observe in these objects as well.

The iron emission line. We observe some weak evidence for the presence of a line with an $EW \sim 20$ eV at 6.8 ± 0.1 keV, consistent with the Kα line from He-like iron. PKS 0558-504 is not unusual among radio-quiet objects in this respect, as similar lines have been observed in many AGN. Bianchi et al. (2009) for example report the detection of such a line with an EW less than 20 eV in at least 12 (broad and narrow line) objects in their sample. The weakness of the line's strength may be easily explained

if the disc is covered by a hot layer which is up-scattering the disc photons to produce the observed soft-excess (see below). If its optical depth is larger than unity, then even if the disc is producing iron lines due to reflection, they will be significantly suppressed by Compton scattering in this layer (Matt et al. 1997).

We do not observe any evidence from iron line emission of neutral material. The 99% upper EW limit for a narrow iron Kα line in the total spectrum of the source is just 11 eV. This is significantly smaller than the EW of ~40 eV that is expected from objects of luminosity $\sim 8 \times 10^{44}$ erg/s (Bianchi et al. 2007). In the case of lines arising from reflection of X-rays from the disc, this result can be explained from the fact that the disc material is highly ionised, as discussed above. But iron lines can also be produced by reprocessing of X-rays from distant, cold Compton-thick matter, as for instance from the putative torus. The lack of a neutral iron Kα line suggests that the covering factor of the Compton-thick torus in this object must be significantly smaller than the covering factor in similar luminosity Seyferts. On the other hand, the absence of this line agrees with the fact that PKS 0558-504 is most probably accreting at a rate higher than $\dot{m}_{\rm Edd}$. Indeed, objects with $\dot{m}$ significantly higher than $\dot{m}_{\rm Edd}$ show lines with an EW which is smaller than 20–10 eV (Bianchi et al. 2007). Perhaps the increase of the opening angle of the torus may then depend mainly on the accretion rate and not just the luminosity of the source.

The soft excess. We found that the soft excess emission below ~2 keV is best explained by a low-temperature (~0.42 keV) Comptonisation component, where the temperature of the seed photons is ~0.11 keV. This agrees with the results of Brinkmann et al. (2004). The seed photons temperature is not consistent with the expected maximum temperature in the innermost region of a Shakura & Sunyaev, optically thick and geometrically thin accretion disc around a $\sim 6 \times 10^7\ M_\odot$ BH (which should be ~15 times smaller than ~0.1 keV in the case when $\dot{m} \sim 0.3\dot{m}_{\rm Edd}$). However, in the case of super-Eddington accretion discs, the accretion flow deviates from the thermodynamic equilibrium, and as a result the accreted gas can be overheated in the central region. Beloborodov (1998) has shown that the maximum temperature in the disc around a massive (Schwarzschild) black hole can be as large as $\sim 10^7$ K, if the accretion rate is 100 times $\dot{m}_{\rm Edd}$. Since the temperature of the gas in the disc determines the emission spectrum to a large extent, it may not be surprising for the spectrum of a disc with a super-Eddington accretion rate to extend up to 0.1 keV or so, as observed.

Furthermore, Kawaguchi (2003) has demonstrated that a hot layer (where Comptonisation becomes important) can be developped in the inner region of super-Eddington discs when $\dot{m} > 10\dot{m}_{\rm Edd}$. Perhaps then, due to its super-Eddington accretion rate, there is a hot layer on top of the disc in PKS 0558-504, which can be identified as the low-temperature Comptonising medium responsible for its soft excess emission. Interestingly, low temperature Comptonisation spectra can also fit well the soft excess emission in two AGN which also have a super-Eddington rate, namely EX J0136.9-3510 and RE J1034+396 (Jon et al. 2009; Middleton et al. 2009). If this is the case, then perhaps the physical origin of the soft excess in these objects may be different from the origin of the same component in NLS1 with a sub-Eddington accretion rate, because we would not expect the presence of hot layers in these objects where significant Comptonisation can distort the underlying disc spectrum.

We also found that both the soft excess flux and shape are variable. Regarding the spectral variability of this component, we found that its spectral shape "hardens" (i.e. it shifts to higher energies) with increasing flux (lower panel in Fig. 11).

According to the model-fit results presented in the previous section, this spectral "hardening" can be explained by a decrease (i.e. flattening) of $\Gamma_{\rm Comp}$ at a constant electron temperature with increasing flux. Since $\Gamma_{\rm Comp}$ depends on the optical depth of the Comptonising medium as well, the $\Gamma_{\rm Comp}$ flattening implies an increase in τ with increasing flux. Similar spectral variations were also reported by Brinkmann et al. (2004), who also attributed them to τ variation.

In physical terms, an increase in the normalisation of the soft excess can be achieved by an increase in the size of the emitting area. Indeed, the radial extent of the hot disc layer, where Comptonisation effects become important, does increases with increasing $\dot{m}$ (i.e. increasing flux) according to Kawaguchi (2003). At the same time the Compton y parameter (which depends on the temperature and the optical depth due to scattering in the hot layer) increases as well, and since $\Gamma \propto y^{-2/9}$ (Beloborodov 1999), $\Gamma_{\rm Comp}$ should flatten with increasing $\dot{m}$, as observed. Consequently, both the shape of the soft excess component and its flux and spectral variations are consistent with the hypothesis that, due to the super-Eddington accretion rate of the source, a hot disc layer exists in the innermost region of PKS 0558-504, which significantly distorts the underlying disc emission. An increase in the accretion rate will result in an increase of the size of the hot layer as well as hence an increase in the flux of the soft excess, and an increase in the Compton y parameter, which will in turn result in the "hardening" of the shape of this component.

The delay between soft and hard band flux variations. Our results suggest that the soft excess flux may lead the hard band X-ray flux variations by ~20 ks. If real, such a correlation cannot be explained by reflection models; therefore this result is another indication that such models cannot account for the soft excess component in PKS 0558-504.

We argued in the paragraph above that the soft excess flux variability may be caused by $\dot{m}$ perturbations. One possible explanation for the correlation and the time delay between soft and hard band variations is that the hard band X-rays are produced at a radius $r_{\rm hard}$, which is smaller than the radius where most of the soft excess emission originates, $r_{\rm soft}$, and the $\dot{m}$ perturbations can propagate from $r_{\rm soft}$ to $r_{\rm hard}$. The time-delay between the soft excess and hard band X-rays could then be identified with the propagation/diffusion time scale of the perturbations, which should be of the order of $t_{\rm diff} \sim r_{\rm soft}/v_r$, where v_r is the radial drift velocity of the accretion flow. For example, according to Kawaguchi (2003), in a $\dot{m} = 100\dot{m}_{\rm Edd}$ source, the hot layer, which could be responsible for the soft excess emission, should extend from $r \sim 100$ to $r \sim 2$ (in units of the Schwarzschild radius). If most of the 0.4–1 keV soft excess photons originate at $r \sim 10$, then $t_{\rm diff} \sim 10$–30 ks. If furthermore the hard X-rays are mainly produced at $r \leq 3$, then the delay we detected could be identified with this $t_{\rm diff}$ value.

We note though that even if this is indeed the case in PKS 0558-504, these $\dot{m}$ perturbations should affect the soft and hard band Comptonising regions in a different way; the soft excess "hardens" while the hard band spectrum "softens" with increasing flux (i.e. $\dot{m}$). If the $\dot{m}$ perturbations mainly affect the optical depth of the scattering media, they do it in such a way that while τ increases in the hot disc layer, it should decrease in the hot corona which is responsible for the hard band X-ray continuum. Clearly, more work is needed to elaborate further on the relation between the soft and hard band spectral and flux variations in PKS 0558-504, and other Seyferts as well.

References

Beloborodov, A. M. 1998, MNRAS, 297, 739
Beloborodov, A. M. 1999, in High Energy Processes in Accreting Black Holes, ASP Conf. Ser., 161, 295
Bentz, M. C., Peterson, B. M., Netzer, H., et al. 2009, ApJ, 697, 160
Bianchi, S., Guainazzi, M., Matt, G., & Fonseca Bonilla, N. 2007, A&A, 467, L19
Bianchi, S., Guainazzi, M., Matt, G., Fonseca Bonilla, N., & Ponti, G. 2009, A&A, 495, 421
Brinkmann, W., Yuan W., & Siebert J. 1997, A&A, 319, 413
Brinkmann, W., Arevalo, P., Gliozzi, M., & Ferrero, E. 2004, A&A, 415, 959.
Brinkmann, W., Papadakis, I. E., Raeth, C., Mimica, P., & Haberl, F. 2005, A&A, 443, 397
Corbin, M. R. 1997, ApJS, 113, 245
Corbin, M. R., & Smith, P. S. 2000, ApJ, 532, 136
Edelson, R. A., & Krolik, J. H. 1988, ApJ, 333, 646
Ehle, M., de la Calle, I., Diaz Trigo, M., et al. 2008, XMM-Newton Users Handbook, http://xmm.esac.esa.int/external/xmm_user_support/documentation/uhb_2.6/
Gliozzi, M., Boller, Th., Brinkmann, W., & Brandt, W. N. 2000, A&A, 356, L17
Gliozzi, M., Brinkmann, W., O'Brien, P. T., et al. 2001, A&A, 365, L128
Gliozzi, M., Papadakis, I. E., & Brinkmann, W. 2007, ApJ, 656, 691
Goodrich, R. W. 1989, ApJ, 342, 224
Grupe, D., Beuermann, K., Mannhein, K., & Thomas, H.-C. 1999, A&A, 350, 805
Haba, Y., Terashima, Y., Kunieda, H., & Ohsuga, K. 2008, PASJ, 60, 487

Jon, C., Done, C., Ward, M., Gierlinski, M., & Mullaney, J. 2009, MNRAS, 398, L16
Kalberla, P. M. W., Burton, W. B., Hartmann, D., et al. 2005, A&A, 440, 775
Kawaguchi, T. 2003, ApJ, 593, 69
Komossa, S., Voges, W., Xu, D., et al. 2006, AJ, 132, 531
Krongold, Y., Nicastro, F., Brickhouse, N. S., et al. 2003, ApJ, 597, 832
Laor, A. 1991, ApJ, 376, 90
Matt, G., Fabian, A. C., & Reynolds, C. S. 1997, MNRAS, 289, 175
Middleton, M., Done, C., Ward, M., Gierlinski, M., & Schurch, N. 2009, MNRAS, 394, 250
Miller, L., Turner, T. J., & Reeves, J. N. 2008, A&A, 483, 437
Miniutti, G., Fabian, A. C., Anabuki, N., et al. 2007, PASJ, 59, 315
Mitsuda, K., Inoue, H., Koyama, K., et al. 1984, PASJ, 36,741
Mushotzki, R. F. 1982, ApJ, 256, 92
O'Brien, P. T., Reeves, J. N., Turner, M. J. L., et al. 2001, A&A, 365, L122
Osterbrock, D. E., & Pogge, R. W. 1985, ApJ, 297, 166
Persson S. E. 1988, ApJ, 330, 751
Petrucci P. O., Haardt F., Maraschi L., et al. 2001, ApJ, 556, 716
Ponti, G., Miniutti, G., Cappi, M., et al. 2006, MNRAS, 368, 903
Remillard, R. A., Bradt, H. V., Buckley, D. A. H., et al. 1986, ApJ, 301, 742
Remillard, R. A., Grossan, B., Bradt, H. V., et al. 1991, Nature, 350, 589
Ross, R. R., & Fabian, A. C. 2005, MNRAS, 358, 211
Siebert, J., Leighly, K. M., Laurent-Muehleisen, S. A., et al. 1999, A&A, 348, 678
Sobolewska, M., & Papadakis, I. E. 2009, MNRAS, 399, 1597
Strüder, L., Briel, U. G., Dennerl, K., et al. 2001, A&A, 365, L18
Taylor, R. D., Uttley, P., & McHardy, I. M. 2003, MNRAS, 342, L31
Titarchuk, L. 1994, ApJ, 434, 313
Turner, T. J., Miller, L., Reeves, J. N., & Kraemer, S. B. 2007, A&A, 475, 121
Ulvestad, J. S., Antonucci, R. R. J., & Goodrich, R. W. 1995, AJ, 109, 81
Vasudevan, R. V., & Fabian, A. C. 2009, MNRAS, 392, 1124
Vaughan, S., Fabian, A. C., & Nandra, K. 2003, MNRAS, 339, 1273
Wang, T., Matsuoka, M., Kubo, H., Mihara, T., & Negoro, H. 2001, ApJ, 554, 233
Yuan, W., Zhou, H. Y., Komossa, S., et al.2008, ApJ, 685, 801
Zycki, P. T., Done, C., & Smith, D. A. 1999, MNRAS, 309, 561